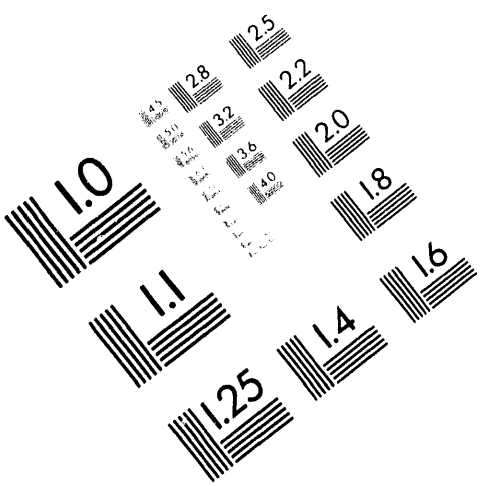

Association for Information and Image Management

1100 Wayne Avenue, Suite 1100
Silver Spring, Maryland 20910

301/587-8202

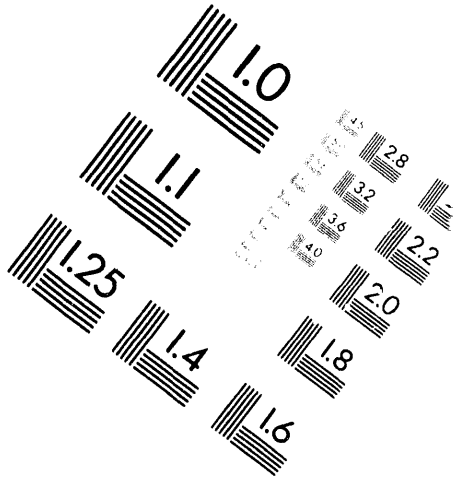

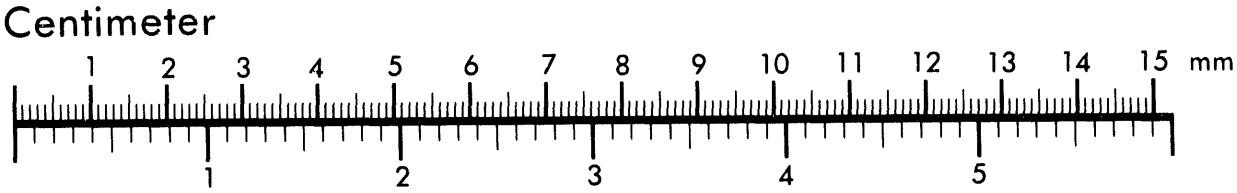

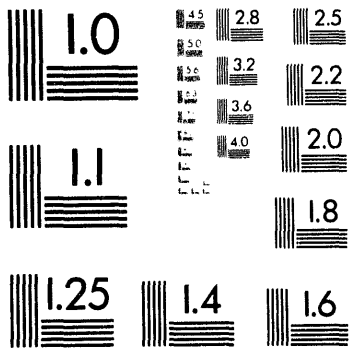

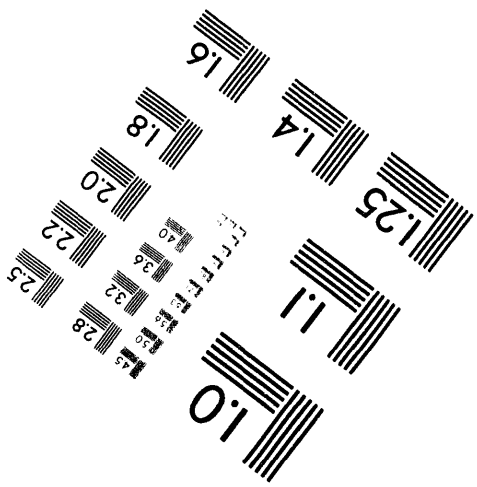

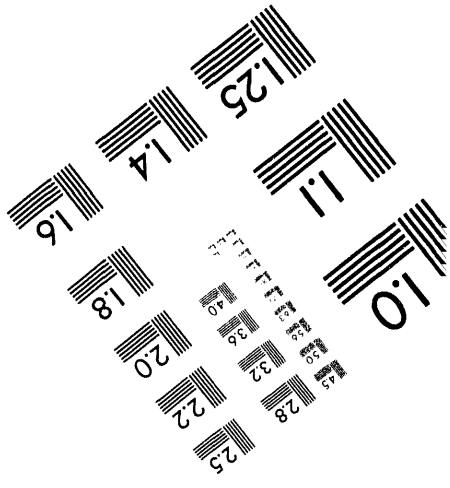

MANUFACTURED TO AIIM STANDARDS
BY APPLIED IMAGE, INC.

1 of 1

Conf-940592--1

UCRL-JC-117488
PREPRINT

Development of X-ray Laser Architectural Components

A. S. Wan, L. B. Da Silva, J. C. Moreno, R. C. Cauble, E. A. Chandler
H. E. Dalhed, S. B. Libby, R. W. Mayle, J. Nilsen, R. P. Ratowsky,
H. A. Scott, and B. Van Wonterghem

This paper was prepared for submittal to the Conference Proceedings
of 4th International Colloquium on X-ray Lasers
Williamsburg, VA
May 16-20, 1994

June 1994

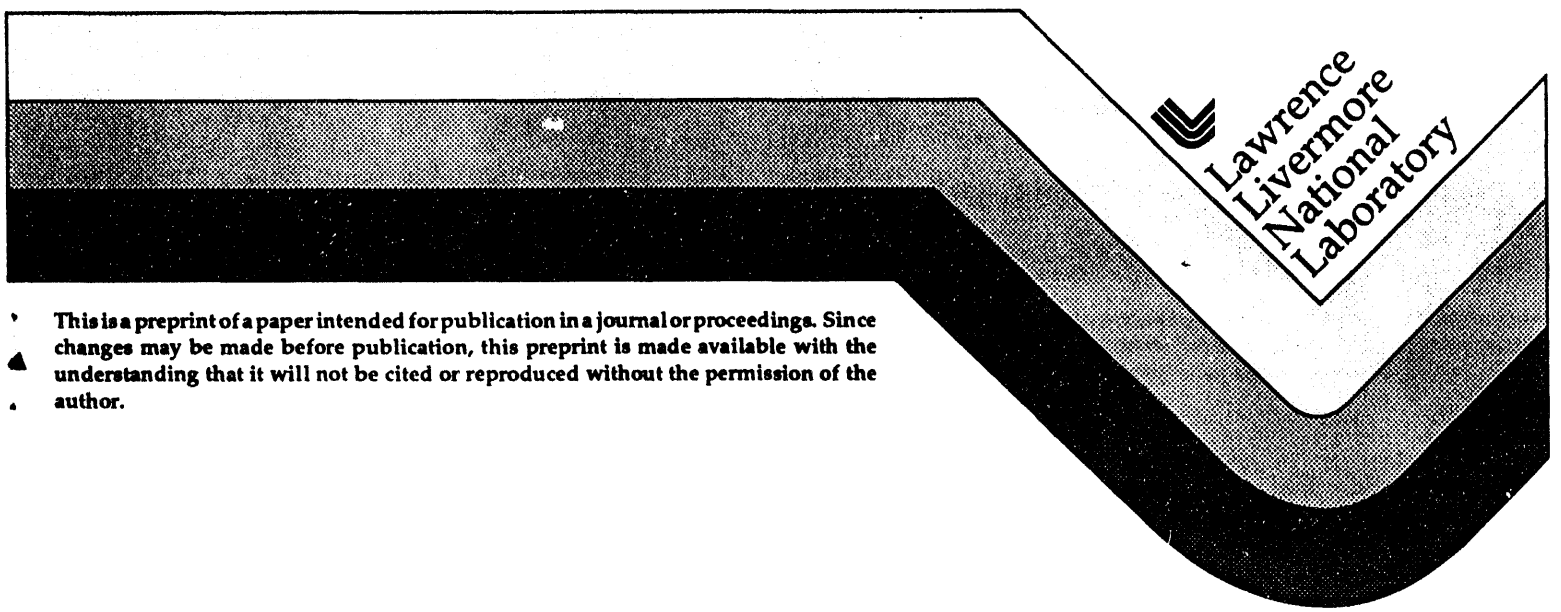

Development of X-ray Laser Architectural Components

A. S. Wan, L. B. Da Silva, J. C. Moreno, R. C. Cauble,
E. A. Chandler, H. E. Dalhed, S. B. Libby, R. W. Mayle,
J. Nilsen, R. P. Ratowsky, H. A. Scott, B. Van Wonterghem

Lawrence Livermore National Laboratory, Livermore, CA 94550

Abstract. This paper describes our recent experimental and computational development of short-pulse, enhanced-coherence, and high-brilliance x-ray lasers (XRLs). We will describe the development of an XRL cavity by injecting laser photons back into an amplifying XRL plasma. Using a combination of LASNEX/GLF/SPECTRE-BEAM3 codes, we obtained good agreement with experimental results. We will describe the adaptive spatial filtering technique used to design small-aperture shaped XRLs with near diffraction-limited output. Finally we will discuss issues concerning the development of high-brilliance XRL architecture, with emphasis on scaling the XRL aperture. Combining these advances in XRL architectural components allows us to develop a short-pulse, high-brilliance, coherent XRL suitable for applications in areas such as biological holography, plasma interferometry, and nonlinear optics.

1. INTRODUCTION

With its short wavelength, controllable pulse duration, high brightness and coherence, the X-ray laser (XRL) is ideally suited as a diagnostic probe to image rapidly evolving (<1 ns) laser-driven plasmas with high electron density (10^{21} cm^{-3} < n_e < 10^{24} cm^{-3}).[1,2] Over the past several year, we have developed a number of XRL applications to probe laser-produced plasmas on the Nova 2-Beam facility at Lawrence Livermore National Laboratory (LLNL), such as radiography,[3] Moiré deflectometry,[3] and 2D interferometry.[2] This paper focuses on the experimental and theoretical development of short-pulse, enhanced-coherence, high-brilliance XRLs for various applications.

Experimentally we use one beam to set up the target plasma to be imaged, which leaves us only one beam to use to generate the XRL, severely limiting our experimental parameters. For our current plasma imaging applications we typically use a 3-cm long exploding-foil Y-XRL[4] with an output energy of ~8 mJ, 200-ps FWHM pulse, ~100 μm diameter source size, 10-mrad divergence, and bandwidth ($\lambda/\Delta\lambda$) of 10^{-4}, which corresponds to a brightness of ~10^{17} W/sr-Å-cm^2. This brightness is equivalent to a 6-GeV blackbody, which overwhelms the self-emission of the target plasma and allows us to use multilayer optics for imaging applications.

Although the Y-XRL has sufficient coherence and brightness for most current imaging applications, we still need to pursue a short-pulse, enhanced-coherence XRL to achieve better spatial resolution and to move toward 3-D holographic applications. Typical laser-produced plasmas have a blowoff velocity of ~10^7 cm/s. Thus, an XRL with a 200-ps FWHM pulse duration yields a spatial resolution of ~20 μm. To obtain higher spatial resolution images of the plasmas, we need to shorten the XRL pulse by another order of magnitude. At LLNL we are developing a short-pulsed XRL using two approaches: traveling wave, which is described in a separate paper in this proceeding,[5] and a short-pulse XRL cavity, which we will describe in detail in Sec. 2 of this paper.

The exploding foil Y-XRL has a temporal coherence of ~30–60 μm, which is sufficient for 2-D interferometry.[2] Beyond the 2-D interferometer, a diffraction-limited XRL can yield 3-D holographic images of ICF capsules. Amplified spontaneous emission becomes diffraction limited as the Fresnel number, N_F, approaches 1. N_F can be defined as $r^2/(\lambda L)$, where L is the XRL length, λ is the wavelength, and r is the radius of the source size. To improve laser coherence, for a fixed λ, we need to either increase L or reduce r. In a refractive medium, L is limited by the maximum refraction length,[6] which can be controlled by reducing ∇n_e,[7] or by curving the XRL target.[8] We can then increase L by using multiple-stage laser architecture [9] or by using multilayer optics. [10]

An alternative approach to obtaining a diffraction-limited XRL is to reduce the XRL aperture. Traditionally the XRL source size is defined by the driving laser optics, with a typical best focus configuration of order of 100 μm FWHM. By controlling the shape of XRLs during plasma expansion and reducing the effective XRL source size using the concept of adaptive spatial filtering, [11] we can obtain a diffraction-limited XRL with a high effective power. In Sec. 3 we will summarize our recent efforts in shaped XRLs.

As XRLs advance beyond plasma imaging applications and toward high deliverable power on target, we need to develop a high brilliance XRL. Brilliance is proportional to the product of intensity and XRL aperture, and inversely proportional to the square of the divergence. In Sec. 4 we will briefly discuss some issues on scaling of the XRL aperture as we march toward a high brilliance XRL architecture. We will summarize and outline our future research direction in Sec. 5.

2. DEVELOPMENT OF AN X-RAY LASER CAVITY

Given the limited experimental flexibility of the Nova 2-Beam facility, one possible technique for achieving a short-pulse yet high-brightness XRL is to use multilayer optics [12] in a cavity configuration. The formation of an XRL cavity relies on the reinjection of XRL photons back into a gain medium using multilayers. Although the half-cavity concept has been tried in the past,[13] mirror damages have limited the performance of the cavity. Our approach on cavity development is to place the injection mirror far away from the XRL to minimize multilayer damage and to use the multiple-pulse [14] configuration on Nova, timed such that the XRL photons produced in earlier pulses will be reinjected and propagate through the gain medium

created by latter pulses. In the following sections we will describe our experimental and theoretical studies of the XRL cavity.

2.1 Experimental Setup and Results

To properly design and understand an XRL cavity we need to know the spatial gain and n_e profiles. The first step of our experimental efforts is to measure the near-field emission profile of the J = 2–1 Y laser line at 155 Å, for a 1-cm-long, 100-μm-thick Y-slab target using the XUV Imaging Diagnostic,[3] which employs an imaging multilayer mirror to look at the near-field spatial emission profile at the chosen wavelength. A spatially defining imaging slit limits the viewing of a 10-μm (in the transverse direction) slice of the plasma in the blow-off direction. With our current setup we have a spatial resolution of order of 2 μm.

In our experiments, we used both available beams to drive two sides (designated as east and west sides) of the Y-slab XRL. The injection mirror is aligned such that the east-side XRL can reinject while the west-side XRL will not couple. The driving Nova pulse shape is a multiple-pulse configuration with four 600-ps gaussian pulses at ~150 TW/cm^2 peak incident intensity at 2ω. The injection mirror is placed at 49.5 cm from the output end of the XRL. We observed little evidence of injection mirror damage during our experiments. The temporal peak-to-peak separation between these four pulses is 1.6 ns, which allows the photons generated by the first pulse to reinject into the gain medium created by the third pulse, and the second pulse to inject into the fourth pulse.

One of the major experimental uncertainties is the damage to the XUV imaging mirror, which is placed at ~30 cm away from the XRL target, caused by the intense optical and broad-band x-radiation from the XRL plasma.[15] This damage limits our ability to see the full effect of the injection. The damage to the imaging mirror is evident as the output intensity weakens as a function of time. But taking the west-side XRL as a reference of non-injected XRL intensity, the output intensity of the east-side XRL is a factor of six or more stronger than the reference intensity. This enhanced intensity agrees well with our estimates and demonstrates the successful coupling between the pulses due to reinjection.

Closer examination of the images of the near-field emission profiles reveal several clues to the properties of this multiple-pulse XRL configuration. The gain regions for all four pulses peak at ~100 μm off the target surface. Furthermore, the gain regions stay at approximately the same positions through all four pulses with no appreciable shifts in position. We also observe some residual gain after the pulses, with this small gain (of order of 1/10 of the peak gain) moving away from the target surface with increasing time. We will compare these features with our numerical simulation of these multi-pulsed XRL plasmas in the next section.

2.2 Modeling of Multiple-Pulse Laser Plasmas

The modeling of XRL plasmas is performed in stages. For collisionally dominated plasmas we can decouple the detailed level populations and line transfer physics from the rest of the problem. We use LASNEX [16] to carry out the laser-deposition

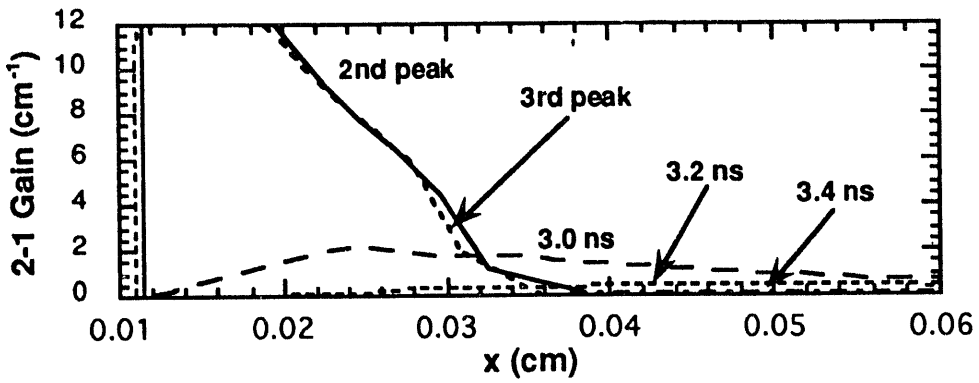

Fig. 1 Spatial gain profiles of Y-XRL peak near the slab surface (0.01 cm) at times corresponding to the peaks of the second and third pulses. Gains inbetween pulses are weaker, with spatial peaks moving away from the slab surface.

and hydrodynamics simulations. From LASNEX we obtain plasma characteristics, such as T_e and n_e, and variables such as mesh positions and velocities. Using our atomic kinetic post-processing code, GLF,[17] we calculate the level populations and line transfer. With the spatial gain and n_e profiles, we can perform ray propagation calculations to match the simulations with actual observable quantities such as laser output intensities. For this purpose we can use SPECTRE, which calculates time-dependent ray trajectories, and BEAM3, which is a 3-D Monte-Carlo ray propagation code to study the effect of refraction and gain saturation.

With the narrow line focus, we can't approximate the plasma expansion by limiting the plasma expansion to a straight 1-D geometry, in which case we calculated T_e ~2.5 keV at the peak of each pulse with an averaged ionization balance between O- and F-like. The plasma remains dense in this geometry. Inbetween pulses the plasma cools to 1–1.5 keV with the majority of the ions at Ne-like. The critical surface moves out as a function of time, which results in a gain profile that moves away from the slab surface as a function of time. Inbetween pulses we still observe large gain due to high T_e and n_e, which can collisionally pump the population inversion. These features clearly disagree with the measured near-field emission profiles.

A much better approximation of the hydrodynamics will be to use a 1-D wedge geometry to represent the 2-D expansion of the laser plasma. An on-axis image of the XRL plasma [18] shows a plasma expansion of order of 20 degree. This expansion is also consistent with 2-D LASNEX simulations of line-focused configuration on slab targets. Each driving laser pulses heats the plasma to a T_e of ~1.5–1.6 keV and burns through slightly beyond an averaged ionization state of Ne-like. Inbetween pulses the plasma expands and cools to ~200-300 eV. The plasma cools and expands after each pulse. Given the long time (1.6 ns) inbetween pulses, by the time the next pulse hits the target, we observe a large n_e reduction, and the majority of the energy will be deposited at a higher n_e region, near the critical surface. Therefore each pulse behaves as if it incidents a new slab target, without large perturbation by the pre-formed plasma in front of the slab, and the plasma behavior reproduces pulse after pulse, which is in agreement with our experimental observation with spatially fixed emission profiles.

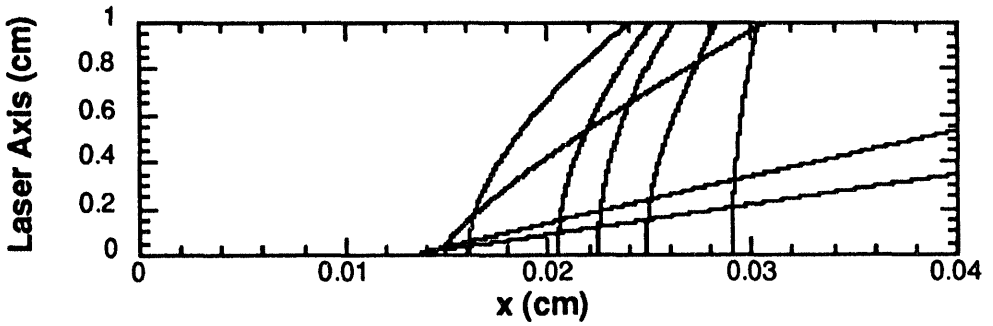

Fig. 2 Ray trajectories across a 1-cm-long Y-XRL, at the peak of the second pulse, showing large refraction for rays launched at the high gain region near the slab surface (0.01 cm), and ~100 μm refraction for the rest of the rays.

We can further postprocess the LASNEX output by using GLF to calculate detailed level populations (and therefore the small signal gains) and line transfer. Figure 1 plots spatial snapshots of the small signal gain profiles of the J = 2–1 line at 155 Å at times between the peaks of the second and third driving pulses. Here we observe strongly peaked gain profiles, with gain >20 cm^{-1} near the slab surface (0.01 cm in Fig. 1). With the reproducible plasma parameters for every pulse, the gain profiles also stay fixed at these positions, in agreement with observation.

With the low T_e inbetween each driving pulse, the plasma recombines past the Ne-like configuration. At these temperatures, collisional excitation rate is low and we observe a factor-of-2 increase in recombination flux from F-like ions to the $3p_{3/2}$ upper laser state. As shown in Fig. 1, the gains inbetween pulses are weak, by about an order of magnitude, and the spatial gain profiles move away from the slab surface with increasing time due to changes in the ionization balance as the plasma cools and expands. These features are also in agreement with our experimental observation and further strengthen our model assumptions.

The one remaining puzzle is the location of the calculated gain, peaking close to the slab surface as compared to our measured emission profiles peaking at 100 μm off the target surface. Several possible mechanisms exist for altering the spatial gain profiles. The effect of radiation trapping, obtained by GLF line transfer calculation, reduces the peak gain, at the peak of the pulses, from ~22 cm^{-1} to ~13 cm^{-1}. But the spatial profiles still peak close to the target surface. We then use SPECTRE and BEAM3 to study the effect of refractive ray propagation on the near-field emission profiles. Figure 2 plots the ray trajectories for a series of parallel rays launched at one end of a 1-cm Y-slab XRL. Rays near the slab traverse across large n_e gradients and are refracted out of the gain region, while rays launched further away from the slab surface face smaller n_e gradients and they refract by about 100 μm as they traverse across a 1-cm region. This 100-μm displacement is in excellent agreement with our experimental observations.

BEAM3 is a 3-D Monte Carlo code that includes the effect of saturation. We can specify the input gain, index of refraction, spontaneous emission rate, and geometries to simulate the Y-XRL. Without the effect of refraction we can recover much of the calculated local gain profile. However, as we turn on refraction, we

observe a similar 100-μm shift in the near-field emission profile with a significant reduction in emission intensity. The combination of both SPECTRE and BEAM3 simulations is our final step in analyzing the Y-slab amplifier. Using all our code capabilities, we obtained a reasonable agreement with the experimental observation.

2.3 Future Research Direction for the XRL Cavity

To produce a short-pulse, enhanced-coherence XRL cavity, we have configured the pulse shape for 100-ps gaussian pulses. We found no evidence of locking with this setup. We also observed very small gain in the first pulse. This is consistent with observations of experiments done at Osaka.[19] Preliminary calculations support the experimental data, showing small gain due to low T_e's with few Ne-like ions. The first pulse, in this configuration, serves to pre-form the plasma to set up the latter pulses. With damage of our imaging mirror, we can't observe locking on the fourth pulse by the XRL photons generated by the second pulse. We will focus our effort on the continued development of the short-pulse XRL cavity in the next set of experiments. We are also planning to measure the change of coherence [20] of Y XRLs with and without reinjection.

3. ENHANCED COHERENCE: ADAPTIVE SPATIAL FILTERING

Instead of letting the driving laser optics define the XRL aperture, the concept of adaptive spatial filtering of an XRL uses geometric shaping to control the laser aperture. This could be in a conical or bowtie-shaped laser. In the unsaturated regime, rays that traverse the longest gain regions have the possibility of attaining the greatest gain lengths (GL) and highest output intensities. The neck of the bowtie laser acts as a narrow spatial filter where the high-GL rays must pass through. These high-GL rays have strong correlation between their angle of tilt and their transverse positions. Rays that travel outside of the bowtie neck achieve lower GLs and are also attenuated by surrounding materials. In a non-refractive and uniform-gain medium, the output of an unsaturated bowtie XRL would be weaker than that of a stripe XRL by the ratio of the neck area to the end area.

In the saturated regime, the coherent power of a bowtie XRL increases by extracting significant power into only a few modes and by eliminating parasitic modes. In saturation the loaded gain depends on the overall intensity pattern in a nonlinear and self-consistent way with the maximum gain located at the neck region, where the adaptive spatial filtering occurs. This effective spatial gain distribution maintains the correlation between ray tilt and transverse position at the laser output end that is needed to achieve high coherent power. Thus the energy content of a saturated XRL preferentially flows through the few Fresnel zones defined by the bowtie neck. In a non-refractive and uniform-gain medium, the output intensity of a bowtie XRL would be weaker than that of a stripe XRL by the ratio of active gain volumes between the two geometries. However the coherent power of a bowtie XRL would be much greater than that of a stripe XRL.

A key issue in the performance of bowtie XRLs is our ability to maintain the bowtie shape during the plasma expansion. One way to fabricate a bowtie XRL is to deposit a bowtie-shaped thin film coating on a thick substrate. The substrate is

made of similar-Z material such that the substrate plasma provides a hydrodynamic tamper to the XRL plasma and maintains the bowtie shape during the lasing period. We have performed a series of numerical studies on the hydrodynamics, kinetics, and lasing properties of a simple stripe-shaped Ge XRL.[11] A series of 2-D LASNEX calculations simulating a line-focused slab XRL and a similar-width stripe XRL shows that a similar-Z hydrodynamic tamper, such as Cu on Ge, can effectively control the XRL plasma expansion to 1-D. Such one-dimensionally expanding plasmas should also provide a flatter transverse n_e profile in the lasing region and reduce the transverse laser divergence.

We have performed a set of experiments comparing a 120-μm line-focused Ge-slab XRL and a 120-μm Ge stripe and bowtie (120-μm ends with 25-μm necks) XRLs deposited on solid Cu substrates. Pinhole camera images contrasting the stripe and slab emission features and imaging of targets at 33.8 Å using a normal-incident multilayer mirror [18] qualitatively confirmed our LASNEX results on the hydrodynamic behaviors of these Ge/Cu plasmas. At or near saturation the stripe XRL intensities are comparable to a line-focused slab XRL. The comparable laser intensities indicate no significant differences in gains and refractive ray propagation between the two XRL configurations. The bowtie XRL intensities were factors of 10–15 lower than the intensities for the stripe and slab XRLs. This intensity difference is likely due to less gain medium of the bowtie configuration and the refractive nature of the plasma medium. X-ray emission spectra in the 8–11-Å range of slab, stripe, and bowtie targets found contributions dominated by Ne-like Ge lines, and a forest of Cu lines ranging from N- to Ne-like. Intensities of Cu and Ge emissions are in agreement with the types of XRLs fielded. The comparable temporal histories of the identified Ne-like Ge 3d and 3s → 2p emission lines indicate comparable ionization histories for the slab and stripe XRLs.

We are planning further characterizations of stripe and bowtie XRLs, such as measurements of small signal gains, plasma expansion characteristics, and coherence. We also have plans to further enhance the bowtie output by varying Nova pulse shapes, using new XRL target designs, and using multiple-staged oscillator-amplifier configurations.

4 SCALING THE XRL APERTURE

To develop a high-brilliance XRL we need to reduce the XRL divergence, increase the intensity, and scale the XRL aperture. Intensity is limited by saturation. In an idealized XRL architecture, we want to maximize the extraction of laser energy by using a small-source-size oscillator, control the divergence by collimating the XRL photons using multilayers or Fresnel zone plates,[21] and scale the aperture using a large-aperture, low-refraction amplifier. In the previous section we have discussed one possible approach of generating a diffraction-limited, small-source-size oscillator using the adaptive spatial filtering technique, and there are many efforts around the world [12,21] trying to develop optics components in the x-ray regime.

In designing an idealized large-aperture XRL amplifier we want to minimize the effect of refraction and maximize the spatial gain such that the amplifier plasma will enhance output intensity while maintaining the optical quality of the x-rays. When a

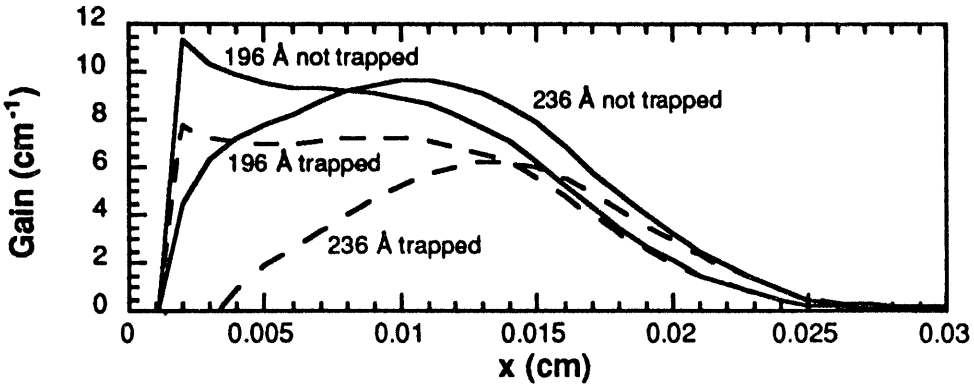

Fig. 3 Effect of trapping on the spatial gain profiles of the Ge 196- and 236-Å line at the center of a 500-μm line-focused slab XRL, as calculated by GLF line-transfer calculations.

prepulse technique is used to pre-form the plasma,[7,19] lasing occurs at region with flatter density gradient and the effect of refraction is reduced. We can also curve the XRL target to match the angle of curvature with the refraction angle.[8] But even if we can develop techniques to minimize the effect of refraction, we still need to address our ability to design a high-gain, large-aperture amplifier. In this section we will address the effect of trapping on the spatial gain profile.

Trapping can be described as a radiative excitation process that pumps the ground-state electrons to the lower laser state, thus reducing the inversion density. Unless the Doppler effect is large enough to shift the frequencies of the emitted photons far from the absorption profile, the effect of trapping depends largely on the ground-state population and the laser aperture. As the aperture increases, the optical depth of the trap line increases, resulting in the trap field buildup at the high-density region, where gain is normally largest for this collisionally excited scheme.

The population inversion, ΔN, is dependent on the populations of the upper and lower laser states, where the lower laser state is adjusted by the statistical weight, g (defined as $g \equiv 2J + 1$), of the upper and lower states:

$$\Delta N = N_{upper} - \left(g_{upper} / g_{lower} \right) N_{lower} ,$$

For the J = 0–1 line, $g_{upper}/g_{lower} = 1/3$, as compared to the J = 2–1 line with $g_{upper}/g_{lower} = 5/3$. Therefore trapping, which populates the lower laser state, favors the J = 0–1 line. To illustrate this trapping effect we simulate a large-aperture XRL using a 500-μm-FWHM line focus on a Ge-slab, with a 600-ps squared pulse at an intensity of 20 TW/cm^2 at 2ω. Figure 3 compares the gain profiles, at 400-ps into the pulse, of the Ge J = 0–1 (196-Å) and J = 2–1 (236-Å) lines at the center of this large-aperture XRL, for trapped and untrapped line-transfer calculations using GLF. Near the slab we observe a large gain reduction of the 236-Å line while the gain of the 196-Å line remains close to the untrapped case.

5. SUMMARY

This paper describes our experimental and theoretical studies of the development of various XRL architectural components for different experimental conditions. We have begun developing a short-pulse XRL cavity, and have obtained good agreement between the measured near-field emission profile and the simulation using a combination of LASNEX/GLF/SPECTRE-BEAM3. In our simulations we have demonstrated the importance of properly modeling the effect of hydrodynamic expansion, atomic physics, and refractive ray propagation. We are also developing a small-source-size oscillator using the concept of adaptive spatial filtering by geometric shaping. Using a bowtie-shaped XRL, we hope to eventually demonstrate a diffraction-limited single-stage XRL. Finally, we addressed issues of refraction and trapping on developing a large-aperture XRL amplifier as the final component of a high-brilliance XRL architecture.

ACKNOWLEDGMENT

Work performed under the auspices of the U. S. DOE by LLNL under contract number W-7405-ENG-48 and is partially supported by the Institute Sponsored Research Program.

REFERENCES

1. See papers in *Proc. of the Applications of X-ray Lasers Workshop*, R. A. London, D. L. Matthews, S. Suckewer, Eds., LLNL Report CONF-9206170 (January 1992).
2. L. B. Da Silva et al., this proceeding.
3. L. B. Da Silva et al., *Proc. Ultrashort Wavelength II, SPIE* **2012**, 158, S. Suckewer, Ed. (1993).
4. L. B. Da Silva et al., *Opt. Lett.* **18**, 1174–1176 (1993).
5. J. C. Moreno et al., this proceeding.
6. R. A. London et al., in *X-Ray Laser 1990*, G. J. Tallents, Ed., 363–370 (IOP Publishing, Bristol and Philadelphia, 1991).
7. J. Nilsen et al., *Phys. Rev. A* **48**, 4682–4685 (1993).
8. Y. Kato et al., *Proc. Ultrashort Wavelength II, SPIE* **2012**, 12, S. Suckewer, Ed. (1993).
9. C. L. S. Lewis, et al., *Opt. Commun.* **91**, 71–76 (1992).
10. M. Key, *Proc. Ultrashort Wavelength II, SPIE* **2012**, 22, S. Suckewer, Ed. (1993).
11. A. S. Wan et al., to be published in *Optical Engineering*.
12. T. Barbee, this proceeding.
13. P. Jaeglé et al., in *X-Ray Laser 1992*, E. E. Fill, Ed., 1–7 (IOP Publishing, Bristol and Philadelphia, 1992).
14. P. L. Hagelstein, *Proc. Short Wavelength Coherent Radiation: Generation and Applications*, R. W. Falcone and J. Kirz, Eds. (1988)
15. B. J. MacGowan et al., *J. X-ray Science and Technol.* **3**, 231–282 (1992).
16. G. B. Zimmerman and W. L. Kruer, *Com. Plasma Phys. and Cont. Fusion* **2**, 51 (1975).
17. H. A. Scott and R. W. Mayle, *Applied Physics B* **58**, 35–43 (1994).
18. J. F. Seely et al., submitted to *Physics of Plasma*.
19. H. Daido et al., this proceeding.
20. J. E. Trebes et al., *Phys. Rev. Lett.* **68**, 588–591 (1992).
21. A. V. Vinogradov, this proceeding.

DATE
FILMED
9/7/94
END